Journal of Systems Engineering and Electronics
Vol. 35, No. 4, August 2024, pp.999 – 1012

Modified filter for mean elements estimation with state jumping

YU Yanjun[1], YUE Chengfei[2,*], LI Huayi[1], WU Yunhua[3], and CHEN Xueqin[1]

1. Research Center of Satellite Technology, Harbin Institute of Technology, Harbin 150001, China;
2. Institute of Space Science and Applied Technology, Harbin Institute of Technology (Shenzhen), Shenzhen 518055, China;
3. College of Astronautics, Nanjing University of Aeronautics and Astronautics, Nanjing 211106, China

Abstract: To investigate the real-time mean orbital elements (MOEs) estimation problem under the influence of state jumping caused by non-fatal spacecraft collision or protective orbit transfer, a modified augmented square-root unscented Kalman filter (MASUKF) is proposed. The MASUKF is composed of sigma points calculation, time update, modified state jumping detection, and measurement update. Compared with the filters used in the existing literature on MOEs estimation, it has three main characteristics. Firstly, the state vector is augmented from six to nine by the added thrust acceleration terms, which makes the filter additionally give the state-jumping-thrust-acceleration estimation. Secondly, the normalized innovation is used for state jumping detection to set detection threshold concisely and make the filter detect various state jumping with low latency. Thirdly, when sate jumping is detected, the covariance matrix inflation will be done, and then an extra time update process will be conducted at this time instance before measurement update. In this way, the relatively large estimation error at the detection moment can significantly decrease. Finally, typical simulations are performed to illustrated the effectiveness of the method.

Keywords: unscented Kalman filter, mean orbital elements (MOEs) estimation, state jumping detection, nonlinear system.

DOI: 10.23919/JSEE.2024.000081

1. Introduction

With the surge in mega-constellations [1,2], researchers pay more attention to autonomous control of satellites. Compared with the satellite formation, the distance between the satellite in the constellation is larger, thus it is more advantageous to use the orbital averaging techniques for the control law design to reduce the influence of high-frequency variations and decrease fuel consumption [3,4]. By using orbital averaging techniques, we can derive the mean orbital element (MOEs) in which the short-term oscillations are filtered out while the long-terms and the secular motions are kept.

Traditionally, MOEs are calculated in the ground station, and will be subsequently sent to the satellite [5]. On the contrary, for a mega-constellation with a large number of satellites, this kind of methods are hard to accomplish. Onboard MOEs estimation is a suitable solution to this problem, using the sensors like global navigation satellite system (GNSS) receiver to generate inputs [6]. Nowadays, there are mainly two types of methods available for onboard MOEs estimation. The first category calculates MOEs analytically or semi-analytically, such as the Kozai theory [7,8], the Brouwer sputnik theory [9], the Liu-Lin method [10], or newer theories, including the methods discussed in [11–15] to name only a few. These methods can be called as the direct mapping (DM) methods, and improve precision by dealing with intricacy orbital dynamic models. However, their sensitivity to the noise and the modeling error make it not the optimal choice. The second type adopts filters [16–19], which can reduce the influence of noise. Wang et al. [20,21] analyzed the performance of the unscented Kalman filter (UKF) and the extended Kalman filter (EKF) on formation flying and investigated the study of computing the differential MOEs using the square-root UKF (SRUKF). Zhong et al. [22] derived the semi-analytical dynamics for osculating orbital elements (OOEs) and MOEs. Then, the spherical simplex SRUKF was used for onboard MOEs estimation based on that dynamics when the satellite maneuver is precisely known. Li et al. [23] gave an onboard MOEs estimation method for geostationary satellites by mixing Jacobi matrix and UKF. The above methods improve the accuracy of the estimation results and are more promising for onboard MOEs estimation.

For the methods mentioned in [20–23], there is an implicit assumption that the maneuvering thrust of the satellite is known and error-free while orbiting. This drawback restricts their application, because when state jumping happens, the satellite usually cannot get the abrupt disturbances that cause state jumping. Consequently, the performance of these filtering methods will

---

Manuscript received March 14, 2023.

*Corresponding author.

This work was supported by National Natural Science Foundation of China (12372045) and Shanghai Aerospace Science and Technology Program (SAST2021-030).

degrade, and may even diverge due to the mismatch between the actual maneuver and the nominal model. Detailly, during iteration of these methods, the propagation of the covariance and the Kalman gain matrix have nothing to do with the residual and finally draw on constant value as demonstrated in [24]. When state jumping occurs, the residuals will increase. However, the covariance and Kalman gain cannot respond to the rapid change of MOEs, and then, the filter diverges. By reconstructing the standard Kalman filter (KF) to cope with unknown inputs, this phenomenon can be mitigated. For instance, conducting state augmentation by adding the maneuver acceleration with covariance matrix inflation. Similar reconstructions are applied when tracking trajectory [25–29] of unknown-maneuvering targets.

Motivated by the problem of estimating the MOEs of a satellite with state-jumping, an MOEs estimator based on the Savitzky-Golay filter with adaptive frame size, maneuvering detector, and multimode switching mechanism was proposed in [30]. Although that estimator can identify state jumping, it cannot estimate the state-jumping-thrust-acceleration and is less accurate during the state jumping period. Thus, in this paper, we propose the modified augmented square-root UKF (MASUKF) by reconstructing the SRUKF in [22] to cope with the state jumping and make up for the above-mentioned problems. The MASUKF is composed of the sigma points calculation, the time update, the state jumping detection, and the measurement update. It has three main specific features. Firstly, augmentation of the state makes the filter additionally give the state-jumping-thrust-acceleration estimation. Secondly, the innovation is normalized and used for state jumping detection. In this way, the thresholds for state jumping detection can be set concisely and the filter can detect various state jumping with low latency. Thirdly, when sate jumping is detected, the covariance matrix inflation will be done, and then the time update process will be re-conducted at this time instance before measurement update to reduce the large estimation error at the detection moment.

The remainder of this paper is organized as follows. Section 2 presents OOEs and theoretical MOEs of low Earth orbit (LEO) satellites and gives the nonlinear measurement and state equations. Section 3 derives the MASUKF for MOEs estimation. Section 4 performs the numerical simulations which compare MASUKF, ASUKF, SUKF, and DM method. The delay time of the state jumping detection is also analyzed. Finally, conclusions are drawn in Section 5.

2. Augmented state and measurement equations

To establish the augmented state and measurement equations, the dynamics and measurement model for small eccentricity LEO satellites are given in this section by choosing rational order terms according to [7,9,22,31–33]. For the sake of simplicity, only J2 perturbation and drag are taken into consideration. In analytical perturbation theory, the terms of perturbation can be decomposed, including the secular, short-periodic, and long-periodic terms. In this paper, the derivative of the MOEs dynamics considers secular terms, long-periodic terms, Gauss variational equations (GVEs), and process noise while the measurements model adds measurement noise and short-periodic terms.

2.1 Augmented state equations

The analytical solution of orbital perturbation is developed based on the GVEs, which come in many forms and allow for both conservative forces and non-conservative forces [31]. The form used in this paper decomposes the forces in the NTW frame. The center of the NTW frame is the satellite. The N axis is perpendicular to W and T. The W axis is in the direction of the angular momentum vector. The T axis is positive in the direction of the velocity vector, and is tangential to the orbit. When $i \neq 0$, $i \neq \pi$, and $0 < e < 1$, the results are

$$\begin{cases} \dfrac{\mathrm{d}a}{\mathrm{d}t} = \dfrac{2\sqrt{\tilde{e}}}{n\sqrt{1-e^2}} a_{\mathrm{T}} \\ \dfrac{\mathrm{d}e}{\mathrm{d}t} = \dfrac{\sqrt{1-e^2}}{na\sqrt{\tilde{e}}} [2(\cos f + e) a_{\mathrm{T}}] - \left(\sqrt{1-e^2}\sin E\right) a_{\mathrm{N}} \\ \dfrac{\mathrm{d}i}{\mathrm{d}t} = \dfrac{r\cos u}{na^2\sqrt{1-e^2}} a_{\mathrm{W}} \\ \dfrac{\mathrm{d}\Omega}{\mathrm{d}t} = \dfrac{r\sin u}{na^2\sqrt{1-e^2}\sin i} a_{\mathrm{W}} \\ \dfrac{\mathrm{d}\omega}{\mathrm{d}t} = \dfrac{\sqrt{1-e^2}}{nae\sqrt{\tilde{e}}} [2a_{\mathrm{T}}\sin f + (\cos E + e) a_{\mathrm{N}}] - \cos i \dfrac{\mathrm{d}\Omega}{\mathrm{d}t} \\ \dfrac{\mathrm{d}M}{\mathrm{d}t} = n - \dfrac{1-e^2}{nae\sqrt{\tilde{e}}} \Bigg[\left(2\sin f + \dfrac{2e^2}{\sqrt{1-e^2}}\sin E\right) a_{\mathrm{T}} + \\ \qquad (\cos E - e) a_{\mathrm{N}}\Bigg] \end{cases} \tag{1}$$

where $\tilde{e} = 1 + 2e\cos f + e^2$, e denotes eccentricity, a denotes semi-major axis, Ω denotes the right ascension of ascending node (RAAN), i denotes inclination, ω denotes the argument of the periapsis, E denotes the eccentric anomaly, M denotes the mean anomaly, f denotes the true anomaly, $u = \omega + f$ denotes the argument of latitude, r denotes the orbital radius, $n = \sqrt{\mu / a^3}$ denotes the mean motion, $\mu = 3.986 \times 10^{14}\ \mathrm{m^3/s^2}$ is the Earth gravitational parameter, a_{N}, a_{T}, and a_{W} are the total acceleration components in NTW coordinate system. With $\boldsymbol{\upsilon} \triangleq [a_{\mathrm{T}}$,

$a_{\rm N}, a_{\rm W}]^{\rm T}$ as the acceleration vector and $\boldsymbol{\alpha} \triangleq [a, e, i, \Omega, \omega, M]^{\rm T}$ as the parametric vector, the GVEs can be written as $\dot{\boldsymbol{\alpha}} = g(\boldsymbol{\alpha}, \boldsymbol{v})$. It can be used to compute the orbital elements variation when $\boldsymbol{v}$ denotes the thrust acceleration imposed on the satellite. Notice that the GVEs are traditionally written in OOEs, but for state equation propagation, the MOEs need to be used instead. This approximation was proved adequate in [32].

In [22], the precise propagation model of MOEs was summarized according to the methods of Kozai and Brouwer [7,9]. The secular and long-periodic terms under J2 perturbation can be written as

$$\begin{cases} \dfrac{{\rm d}a_{\rm sec}}{{\rm d}t} = \dfrac{{\rm d}e_{\rm sec}}{{\rm d}t} = \dfrac{{\rm d}i_{\rm sec}}{{\rm d}t} = 0 \\ \dfrac{{\rm d}\Omega_{\rm sec}}{{\rm d}t} = -\dfrac{3J_2 n\cos i}{2}\left(\dfrac{R_E}{p}\right)^2 + \dfrac{3J_2^2 n\cos i}{8}\left(\dfrac{R_E}{p}\right)^4\Big[-9- \\ \qquad e^2 - 6\sqrt{1-e^2} + \sin^2 i\left(10 - \dfrac{5e^2}{4} + 9\sqrt{1-e^2}\right)\Big] \\ \dfrac{{\rm d}\omega_{\rm sec}}{{\rm d}t} = \dfrac{3J_2 n}{2}\left(\dfrac{R_E}{p}\right)^2\left(2 - \dfrac{5}{2}\sin^2 i\right) + \dfrac{3J_2^2 n}{128}\left(\dfrac{R_E}{p}\right)^4 \cdot \\ \qquad \Big[384 + 56e^2 + 192\sqrt{1-e^2} - \sin^2 i\left(824 + 36e^2 + \right. \\ \qquad \left. 528\sqrt{1-e^2}\right) + \sin^4 i\left(430 - 45e^2 + 360\sqrt{1-e^2}\right)\Big] \\ \dfrac{{\rm d}M_{\rm sec}}{{\rm d}t} = \dfrac{3J_2 n\sqrt{1-e^2}}{2}\left(\dfrac{R_E}{p}\right)^2\left(1 - \dfrac{3}{2}\sin^2 i\right) + \\ \qquad \dfrac{J_2^2 n\sqrt{1-e^2}}{128}\left(\dfrac{R_E}{p}\right)^4\Big[192\sqrt{1-e^2} - 120\left(1-e^2\right) + \\ \qquad 360 + \sin^2 i\left(120\left(1-e^2\right) - 576\sqrt{1-e^2} - 720\right) + \\ \qquad \sin^4 i\left(75\left(1-e^2\right) + 432\sqrt{1-e^2} + 315\right)\Big] \end{cases} \tag{2}$$

where R_E is Earth radius, $J_2 = 1.082\,64 \times 10^{-3}$, $p = a(1-e^2)$ is the semilatus rectum.

$$\begin{cases} \dfrac{{\rm d}a_{\rm long}}{{\rm d}t} = 0 \\ \dfrac{{\rm d}e_{\rm long}}{{\rm d}t} = -\dfrac{3J_2^2 R_e^4 ne}{32\tilde{p}^4}\left(1-e^2\right)\left(15\cos^2 i - 1\right)\sin^2 i\sin(2\omega) \\ \dfrac{{\rm d}i_{\rm long}}{{\rm d}t} = \dfrac{3J_2^2 R_e^4 ne^2}{64p^4}\left(15\cos^2 i - 1\right)\sin(2i)\sin(2\omega) \\ \dfrac{{\rm d}\Omega_{\rm long}}{{\rm d}t} = -\dfrac{3J_2^2 R_e^4 ne^2}{16p^4}\left(15\cos^2 i - 8\right)\cos i\cos(2\omega) \\ \dfrac{{\rm d}\omega_{\rm long}}{{\rm d}t} = \dfrac{3J_2^2 R_e^4 n}{64p^4}\Big[30\cos^4 i - 32\cos^2 i + 2 + \\ \qquad e^2\left(135\cos^4 i - 112\cos^2 i + 5\right)\Big]\cos(2\omega) \\ \dfrac{{\rm d}M_{\rm long}}{{\rm d}t} = -\dfrac{3J_2^2 R_e^4 n\sqrt{1-e^2}}{64p^4}\left(2 - 5e^2\right) \cdot \\ \qquad \left(1 - 16\cos^2 i + 15\cos^4 i\right)\cos(2\omega) \end{cases} \tag{3}$$

The specific force due to atmospheric drag can be modeled as mentioned in [33], which assumes the atmosphere to be spherical and co-rotating with the Earth. The drag force per unit mass is as follows:

$$\boldsymbol{F}_{\rm drag} = -\frac{1}{2}\frac{SC_{\rm D}}{m}\rho(\boldsymbol{v}_{\rm sat} - \boldsymbol{v}_{\rm atm})\|\boldsymbol{v}_{\rm sat} - \boldsymbol{v}_{\rm atm}\| \tag{4}$$

where $C_{\rm D}$ is the drag coefficient, m denotes satellite mass, ρ denotes the atmospheric density, S denotes the cross-sectional reference area, $\boldsymbol{v}_{\rm sat}$ denotes the satellite velocity, $\boldsymbol{v}_{\rm atm} = [0, 0, \omega_e]^{\rm T} \times \boldsymbol{r}$ denotes the atmospheric velocity, and $\boldsymbol{r}$ is the position vector of the satellite. The angular velocity of the Earth is $\omega_e = 7.292\,115\,855\,3 \times 10^{-5}$ rad/s. To reflect the major changes of the LEO atmosphere density and get the analytical solution, the exponential atmosphere model is used herein:

$$\rho = \rho_0 \exp\left(\frac{-ae}{H}\right)\sum_{k=0}^{\infty}\frac{1}{k!}\left(\frac{ae\cos E}{H}\right)^k \tag{5}$$

where H is the density scale height of the atmosphere, ρ_0 denotes the atmospheric density at radius r_0. Then, as mentioned in [22], the secular and the long-periodic terms of the atmosphere drag can be given by

$$\begin{cases} \dfrac{{\rm d}a_{\rm drag,sec}}{{\rm d}t} = -K_1\rho_0 na^2\left(1 + H_a + \dfrac{ae^2}{H} + O\left(e^3\right)\right)e_H \\ \dfrac{{\rm d}e_{\rm drag,sec}}{{\rm d}t} = -K_1\rho_0 na\left(\dfrac{e}{2} + \dfrac{ae}{2H} + O\left(e^3\right)\right)e_H \\ \dfrac{{\rm d}i_{\rm drag,sec}}{{\rm d}t} = -\dfrac{K_2\rho_0 a\sin i}{4}\left(1 + H_a - \dfrac{ae^2}{H} + O\left(e^3\right)\right)e_H \\ \dfrac{{\rm d}\Omega_{\rm drag,sec}}{{\rm d}t} = \dfrac{{\rm d}\omega_{\rm drag,sec}}{{\rm d}t} = 0 \\ \dfrac{{\rm d}M_{\rm drag,sec}}{{\rm d}t} = \dfrac{3K_1\rho_0 n^2 a}{4}\left(1 + H_a + \dfrac{ae^2}{H} + O\left(e^3\right)\right)e_H \end{cases}, \tag{6}$$

$$\begin{cases} \dfrac{{\rm d}a_{\rm drag,long}}{{\rm d}t} = \dfrac{{\rm d}e_{\rm drag,long}}{{\rm d}t} = \dfrac{{\rm d}M_{\rm drag,long}}{{\rm d}t} = 0 \\ \dfrac{{\rm d}i_{\rm drag,long}}{{\rm d}t} = -\dfrac{1}{4}K_2\rho_0 a\sin i\left[H_b\cos(2\omega) + O\left(e^3\right)\right]e_H \\ \dfrac{{\rm d}\Omega_{\rm drag,long}}{{\rm d}t} = -\dfrac{1}{4}K_2\rho_0 a\left[H_b\sin(2\omega) + O\left(e^3\right)\right]e_H \\ \dfrac{{\rm d}\omega_{\rm drag,long}}{{\rm d}t} = -\cos i \cdot \dfrac{{\rm d}\Omega_{\rm drag,long}}{{\rm d}t} \end{cases}, \tag{7}$$

where $H_a = \dfrac{3e^2}{4} + \dfrac{a^2e^2}{4H^2}$, $K_1 = (C_D S_1/m)Q$, $K_2 = (C_D S_2/m)\omega_e\sqrt{Q}$, $e_H = \exp\left(\dfrac{r_{P_0} - a}{H}\right)$, $H_b = \dfrac{11e^2}{8} - \dfrac{ae^2}{H} + \dfrac{a^2e^2}{8H^2}$, $Q = (1 - r_P\omega_e\cos i/v_P)^2$, S_1 and S_2 are the cross-sectional areas perpendicular to the tangential and subnormal directions, respectively. r_P and v_P represent the perigee distance and the perigee velocity magnitude, respectively. $O(e^k)$ represents the small quantity whose magnitude is smaller than e^k.

Thus, by taking the influence of thrusts, J2 perturbation, drag and process noise into consideration, the MOEs dynamics of the satellite can be expressed as follows:

$$\dot{\bar{\boldsymbol{\alpha}}} = \dot{\boldsymbol{\alpha}}_{\text{sec}}(\bar{\boldsymbol{\alpha}}) + \dot{\boldsymbol{\alpha}}_{\text{long}}(\bar{\boldsymbol{\alpha}}) + \dot{\boldsymbol{\alpha}}_{\text{drag,sec}}(\bar{\boldsymbol{\alpha}}) + \dot{\boldsymbol{\alpha}}_{\text{drag,long}}(\bar{\boldsymbol{\alpha}}) + \mathrm{g}(\bar{\boldsymbol{\alpha}}, \boldsymbol{\upsilon}_{\text{sj}}) \tag{8}$$

where $\dot{\boldsymbol{\alpha}}_{\text{sec}}(\bar{\boldsymbol{\alpha}})$ and $\dot{\boldsymbol{\alpha}}_{\text{long}}(\bar{\boldsymbol{\alpha}})$ are the secular and long-periodic terms of J2 perturbation, respectively. The secular and long-periodic terms of the atmosphere drag are denoted by $\dot{\bar{\boldsymbol{\alpha}}}_{\text{drag,sec}}(\bar{\boldsymbol{\alpha}})$ and $\dot{\bar{\boldsymbol{\alpha}}}_{\text{drag,long}}(\bar{\boldsymbol{\alpha}})$, respectively. The vector $\boldsymbol{\upsilon}_{\text{sj}}$ denotes the state-jumping-thrust-acceleration, $g(\bar{\boldsymbol{\alpha}}, \boldsymbol{\upsilon}_{\text{sj}})$ is used to involve the influence of the state jumping.

To cope with the state jumping, state-augment is done by combining the rate of the state-jumping-thrust-acceleration, and the modeling error is approximated as Gaussian white noise:

$$\dot{\boldsymbol{x}} = \begin{bmatrix} \dot{\bar{\boldsymbol{\alpha}}} + \boldsymbol{W}_1 \\ \dot{\boldsymbol{\upsilon}}_{\text{sj}} \end{bmatrix} = \begin{bmatrix} \dot{\bar{\boldsymbol{\alpha}}} + \boldsymbol{W}_1 \\ \boldsymbol{W}_2 \end{bmatrix} \tag{9}$$

where $\boldsymbol{x}$ indicates the state vector, $\dot{\boldsymbol{\upsilon}}_{\text{sj}}$ denotes the rate of the state-jumping-thrust-acceleration, and the vector $\boldsymbol{W}_1$ denotes the process noise, which is the reflection of modeling uncertainties. $\boldsymbol{W}_1$ is assumed as the white noise with power spectral density $\boldsymbol{Q}_1$. The rate of the state-jumping-thrust-acceleration is assumed as a Markov process $\dot{\boldsymbol{\upsilon}}_{\text{s}} = \boldsymbol{W}_2$ and the white noise vector $\boldsymbol{W}_2$ is with power spectral density $\boldsymbol{Q}_2$, which means the state-jumping-thrust-acceleration does not change drastically. This is a reasonable assumption because when a satellite with state jumping is considered, the acceleration usually does not change drastically except at the start and the end of the state jumping [26].

2.2 Measurements modeling

Adequate measurements are required for MOEs estimation. The onboard sensors like the GNSS receiver can receive the instantaneous position, velocity, and time information of the satellite. These can be converted to the OOEs by nonlinear conversion. Thus, the measurements can be modeled in the form of OOEs:

$$\boldsymbol{\alpha}_{\text{ob}} = \bar{\boldsymbol{\alpha}} + \boldsymbol{\alpha}_{\text{short}}(\bar{\boldsymbol{\alpha}}) + \boldsymbol{\alpha}_{\text{drag,short}}(\bar{\boldsymbol{\alpha}}) + \boldsymbol{V} \tag{10}$$

where vector $\boldsymbol{V}$ denotes the measurement noise, which can be calculated by the nonlinear mapping among inertial position, velocity, and OOEs through Monte Carlo simulation. $\boldsymbol{\alpha}_{\text{short}}(\bar{\boldsymbol{\alpha}})$ denotes the short-periodic terms under J2 perturbation and $\boldsymbol{\alpha}_{\text{drag,short}}(\bar{\boldsymbol{\alpha}})$ denotes the short-periodic terms caused by drag. The analytical short-periodic terms of the J2 perturbation and the drag [22] are as follows:

$$\begin{cases} a_{\text{short}} = J_2 \dfrac{R_E^2}{a} \left\{ \left(1 - \dfrac{3}{2}\sin^2 i\right)\left[\left(\dfrac{a}{r}\right)^3 - \left(1 - e^2\right)^{-\frac{3}{2}}\right] + \dfrac{3}{2}\sin^2 i \left(\dfrac{a}{r}\right)^3 \cos 2(\omega + f) \right\} \\ e_{\text{short}} = \dfrac{1 - e^2}{e}\left(\dfrac{1}{2a} a_{\text{short}} - i_{\text{short}} \tan i\right) \\ i_{\text{short}} = \dfrac{3J_2 \sin 2i}{8}\left(\dfrac{R_E}{p}\right)^2 \left[\cos 2(\omega + f) + e\cos(2\omega + f) + \dfrac{e}{3}\cos(2\omega + 3f)\right] \\ \varOmega_{\text{short}} = -\dfrac{3J_2 \cos i}{2}\left(\dfrac{R_E}{p}\right)^2 \left[f - M + e\sin f - \dfrac{1}{2}\sin 2(\omega + f) - \dfrac{e}{2}\sin(2\omega + f) - \dfrac{e}{6}\sin(2\omega + 3f)\right] \\ \omega_{\text{short}} = \dfrac{3J_2}{4}\left(\dfrac{R_E}{p}\right)^2 \left\{\left(4 - 5\sin^2 i\right)(f - M + e\sin f) + \left(2 - 3\sin^2 i\right)\left[\left(\dfrac{1}{e} - \dfrac{e}{4}\right)\sin f + \dfrac{1}{2}\sin(2f) + \dfrac{e}{12}\sin(3f)\right] - \right. \\ \qquad \left[\dfrac{1}{2e}\sin^2 i + \left(1 - \dfrac{15}{8}\sin^2 i\right)e\right]\sin(f + 2\omega) + \dfrac{e}{8}\sin^2 i \sin(f - 2\omega) - \left(1 - \dfrac{5}{2}\sin^2 i\right)\sin 2(\omega + f) + \dfrac{3}{4}\sin^2 i \sin(2\omega + 4f) + \\ \qquad \left. \left[\dfrac{7}{6e}\sin^2 i - \left(\dfrac{1}{3} - \dfrac{19}{24}\sin^2 i\right)e\right]\sin(2\omega + 3f) + \dfrac{e}{8}\sin^2 i \sin(2\omega + 5f)\right\} \\ M_{\text{short}} = -\dfrac{3J_2}{2}\left(\dfrac{R_E}{p}\right)^2 \dfrac{\sqrt{1 - e^2}}{e}\left\{\left(1 - \dfrac{3}{2}\sin^2 i\right)\left(\sin f - \dfrac{e^2}{4}\sin f + \dfrac{e}{2}\sin(2f) + \dfrac{e^2}{12}\sin(3f)\right) - \right. \\ \qquad \left. \sin^2 i\left[\left(\dfrac{1}{4} + \dfrac{5}{16}e^2\right)\sin(2\omega + f) + \dfrac{e^2}{16}\sin(2\omega - f) - \left(\dfrac{7}{12} - \dfrac{e^2}{48}\right)\sin(2\omega + 4f) - \dfrac{e^2}{16}\sin(2\omega + 5f)\right]\right\} \end{cases}, \tag{11}$$

$$\left\{\begin{array}{l}
a_{\mathrm{drag,short}}=-K_1\rho_0 a^2 e_H\left[\left(3+\dfrac{a}{H}\right)e\sin M+\left(\dfrac{15}{8}+\dfrac{a}{H}+\dfrac{a^2}{8H^2}\right)e^2\sin(2M)+O\left(e^3\right)\right]\\
e_{\mathrm{drag,short}}=-K_1\rho_0 a e_H\left\{\left[1-\left(\dfrac{1}{2}-\dfrac{a}{H}-\dfrac{3a^2}{8H^2}\right)e^2\right]\sin M+\left(\dfrac{3}{4}+\dfrac{a}{4H}\right)e\sin(2M)+\left[\dfrac{2}{3}+\dfrac{a}{3H}+\dfrac{a^2}{24H^2}\right]e^2\sin(3M)+O\left(e^3\right)\right\}\\
i_{\mathrm{drag,short}}=-\dfrac{K_2\rho_0 a\sin i}{4n}e_H\left\{\left(\dfrac{a}{H}-1\right)e\sin M+\left(\dfrac{a}{2H}-\dfrac{5}{2}\right)e\sin(M+2\omega)+\left[\dfrac{1}{2}+\left(\dfrac{a^2}{8H^2}-\dfrac{a}{2H}-\dfrac{13}{8}\right)e^2\right]\sin(2M+2\omega)+\right.\\
\qquad\left.\left(\dfrac{a^2}{8H^2}-\dfrac{3}{8}\right)e^2\sin(2M)+\left(\dfrac{a}{6H}+\dfrac{1}{2}\right)e\sin(3M+2\omega)+\left(\dfrac{a^2}{32H^2}+\dfrac{a}{4H}+\dfrac{15}{32}\right)e^2\sin(4M+2\omega)+O\left(e^3\right)\right\}\\
\varOmega_{\mathrm{drag,short}}=\dfrac{K_2\rho_0 a}{8n}e_H\left\{\left(\dfrac{a^2}{16H^2}+\dfrac{a}{2H}+\dfrac{15}{16}\right)e^2\cos(4M+2\omega)+\left(\dfrac{a}{3H}+1\right)e\cos(3M+2\omega)+\right.\\
\qquad\left.\left[1+\left(\dfrac{a^2}{4H^2}-\dfrac{a}{H}-\dfrac{13}{4}\right)e^2\right]\cos(2M+2\omega)+\left(\dfrac{a}{H}-5\right)e\cos(M+2\omega)+O\left(e^3\right)\right\}\\
\omega_{\mathrm{drag,short}}=K_1\rho_0 a e_H\left\{\left[\dfrac{1}{e}+\left(\dfrac{a^2}{8H^2-1}\right)e\right]\cos M+\left(\dfrac{a^2}{24H^2}+\dfrac{a}{3H}+\dfrac{2}{3}\right)e\cos(3M)+\right.\\
\qquad\left[\dfrac{a}{4H}+\dfrac{3}{4}+\left(\dfrac{a^3}{48H^3}+\dfrac{a^2}{16H^2}-\dfrac{5a}{16H}-\dfrac{43}{48}\right)e^2\right]\cos(2M)+\\
\qquad\left.\left(\dfrac{a^3}{192H^3}+\dfrac{5a^2}{64H^2}-\dfrac{25a}{64H}-\dfrac{139}{192}\right)e^2\cos(4M)+O\left(e^3\right)\right\}-\varOmega_{\mathrm{drag,short}}\cos i\\
M_{\mathrm{drag,short}}=-K_1\rho_0 a\left\{\left[\dfrac{1}{e}+\left(\dfrac{a^2}{8H^2}+\dfrac{3a}{2H}+4\right)e\right]\cos M+\left(\dfrac{a^2}{24H^2}+\dfrac{a}{3H}+\dfrac{2}{3}\right)e\cos(3M)+\right.\\
\qquad\left[\dfrac{a}{4H}+\dfrac{3}{4}+\left(\dfrac{a^3}{48H^3}+\dfrac{5a^2}{32H^2}+\dfrac{9a}{16H}+\dfrac{61}{96}\right)e^2\right]\cos(2M)+\\
\qquad\left.\left(\dfrac{a^3}{192H^3}+\dfrac{5a^2}{64H^2}+\dfrac{25a}{64H}+\dfrac{139}{192}\right)e^2\cos(4M)+O\left(e^3\right)\right\}e_H
\end{array}\right. . \tag{12}$$

Obviously, (9) and (10) are the nonlinear state and measurement equations, which adhere to the form:

$$\left\{\begin{array}{l}\dot{\boldsymbol{x}}(t_k)=\boldsymbol{f}_{\mathrm{c}}[\boldsymbol{x}(t_k),t_k]+\boldsymbol{W}(t_k)\\ \boldsymbol{y}(t_k)=\boldsymbol{h}[\boldsymbol{x}(t_k)]+\boldsymbol{V}(t_k)\end{array}\right. \tag{13}$$

where $\boldsymbol{y}\equiv\boldsymbol{\alpha}_{\mathrm{ob}}$ indicates the measurement vector.

3. MOEs estimator

As mentioned in Section 1, the KF method cannot give an ideal result when estimating the MOEs of the satellite with state jumping. In order to tolerate the mismatch caused by state jumping, we propose the MASUKF based on the spherical simplex SRUKF mentioned in [22]. The MASUKF introduces the state-augment, innovation-based detection, and the timely covariance matrix inflation to cope with the state jumping. For completeness, this paper elaborates the main steps required to implement MOE estimation based on MASUKF.

3.1 Sigma points selection

The UKF-based algorithm needs to select a set of sampling points according to unscented transformation, also known as sigma sampling points. Moreover, the calculation amount of the UKF-based filtering algorithm is proportional to the number of sigma points. To achieve onboard applications, it is essential to reduce the amount of calculation while maintaining the accuracy of the filtering algorithm. For an n_{s}-dimensional space, the spherical simplex sigma-point selection strategy requires $n_{\mathrm{s}}+2$ sigma points, and has the same predictive capability as the truncated second order filter like the traditional symmetrical sampling strategy that requires $2n_{\mathrm{s}}+2$ sampling points [34]. Thus, the spherical simplex unscented transform is preferable. The point selection method for an n_{s}-dimensional system is as follows:

(i) Select the weight for the points lie on the hypersphere centered at the origin ($i_{\mathrm{s}}\neq 0$) and the point at the origin ($i_{\mathrm{s}}=0$) by

$$\left\{\begin{array}{l}0\leqslant W_0\leqslant 1,\ \ i_{\mathrm{s}}=0\\ W_{i_{\mathrm{s}}}=(1-W_0)/(n_{\mathrm{s}}+1),\ \ i_{\mathrm{s}}\neq 0\end{array}\right. . \tag{14}$$

(ii) Use the scaled unscented transformation to adjust the weights:

$$w_{i_{\mathrm{s}}}=\left\{\begin{array}{l}1+(W_0-1)/\sigma^2,\ \ i_{\mathrm{s}}=0\\ W_{i_{\mathrm{s}}}/\sigma^2,\ \ i_{\mathrm{s}}\neq 0\end{array}\right. \tag{15}$$

where $\sigma\in(0,1]$ denotes the scaling parameter.

(iii) Initialize the vector sequence:

$$\begin{cases} \boldsymbol{Z}_0^1 = [0] \\ \boldsymbol{Z}_1^1 = \left[-\dfrac{1}{\sqrt{2w_1}}\right] \\ \boldsymbol{Z}_2^1 = \left[\dfrac{1}{\sqrt{2w_1}}\right] \end{cases}. \tag{16}$$

(iv) Extend the vector for $j_s = 2,3,\cdots,n_s$ by

$$\boldsymbol{Z}_{i_s}^{j_s} = \begin{cases} \begin{bmatrix} \boldsymbol{Z}_0^{j_s-1} \\ 0 \end{bmatrix}, & i_s = 0 \\ \begin{bmatrix} \boldsymbol{Z}_{i_s}^{j_s-1} \\ -1/\sqrt{j_s(j_s+1)w_1} \end{bmatrix}, & i_s = 1,2,\cdots,j_s \\ \begin{bmatrix} \boldsymbol{0}_{j_s-1} \\ j_s/\sqrt{j_s(j_s+1)w_1} \end{bmatrix}, & i_s = j_s+1 \end{cases} \tag{17}$$

(v) To incorporate higher-order information, the relevant weights are defined as follows:

$$\begin{cases} w_0^{m_s} = w_0, \ i_s = 0 \\ w_0^c = w_0 + (1-\sigma^2+\beta), \ i_s = 0 \\ w_{i_s}^{m_s} = w_{i_s}^c = w_{i_s}, \ i_s = 1,2,\cdots,n_s+1 \end{cases} \tag{18}$$

where parameter β affects the weight of the 0th sigma point for the covariance calculation.

3.2 Time update

Before introducing the time update process, some mathematical relationships and notations need to be introduced. Let $\boldsymbol{P}$ be the error covariance and $\boldsymbol{S}$ be the square root of $\boldsymbol{P}$:

$$\boldsymbol{P} = \boldsymbol{S}^{\mathrm{T}}\boldsymbol{S}. \tag{19}$$

The covariance matrix can be replaced by the respective square roots to improve numerical stability. The MASUKF is composed of three steps (Subsection 3.2–Subsection 3.4) at each time instant t_k.

Assume that the estimated state vector $\hat{\boldsymbol{x}}_{k-1/k-1}$ and the square root of the covariance matrix $\boldsymbol{S}_{k-1/k-1}$ of the previous $k-1$ iteration are known. Then, the sigma points for time t_k can be calculated through (20). The initial value of the state vector and the covariance matrix are $\hat{\boldsymbol{x}}_{0/0} = \mathrm{E}[\boldsymbol{x}_{0/0}]$ and $\boldsymbol{S}_{0/0} = \mathrm{chol}\left(\mathrm{E}[\boldsymbol{x}_{0/0} - \hat{\boldsymbol{x}}_{0/0}][\boldsymbol{x}_{0/0} - \hat{\boldsymbol{x}}_{0/0}]^{\mathrm{T}}\right)$, respectively. The function $\mathrm{chol}(\cdot)$ denotes the Cholesky factorization:

$$\boldsymbol{\chi}_{i_s,k-1/k-1} = \boldsymbol{S}_{k-1/k-1}\boldsymbol{Z}_{i_s} + \hat{\boldsymbol{x}}_{k-1/k-1}. \tag{20}$$

The time update equations are written as follows:

$$\dot{\boldsymbol{\chi}}_{i_s,k-1/k-1} = \boldsymbol{f}_c(\boldsymbol{\chi}_{i_s,k-1/k-1}, t_{k-1}) \tag{21}$$

where $\boldsymbol{\chi}_{i_s,k/k-1}$ can be obtained through the Runge-Kutta integration. The predicted state vector $\hat{\boldsymbol{x}}_{k/k-1}$ and the predicted error covariance square root $\boldsymbol{S}_{k/k-1}$ can be computed by

$$\hat{\boldsymbol{x}}_{k/k-1} = \sum_{i_s=0}^{n_s+1} w_{i_s}^{m_s}\boldsymbol{\chi}_{i_s,k/k-1}, \tag{22}$$

$$\boldsymbol{S}_{k/k-1} = \mathrm{qr}\left(\left[\sqrt{w_1^c}\left(\boldsymbol{\chi}_{1:n_s+1,k/k-1} - \hat{\boldsymbol{x}}_{k/k-1}\right), \sqrt{\boldsymbol{Q}_k}\right]\right), \tag{23}$$

where $\mathrm{qr}(\cdot)$ denotes the QR decomposition; $\boldsymbol{Q}_k$ denotes the process noise covariance and can be determined according to $\boldsymbol{Q}_1$ and $\boldsymbol{Q}_2$.

The predicted sigma points can be computed by $\hat{\boldsymbol{x}}_{k/k-1}$ and $\boldsymbol{S}_{k/k-1}$:

$$\boldsymbol{\chi}_{i_s,k/k-1} = \boldsymbol{S}_{k/k-1}\boldsymbol{Z}_{i_s} + \hat{\boldsymbol{x}}_{k/k-1}. \tag{24}$$

The predicted sigma points can be propagated through $\boldsymbol{y}_{i_s,k/k-1} = \boldsymbol{h}(\boldsymbol{\chi}_{i_s,k/k-1})$ to get the predicted measurements:

$$\hat{\boldsymbol{y}}_{k/k-1} = \sum_{i_s=0}^{n_s+1} w_{i_s}^{m_s}\boldsymbol{y}_{i_s,k/k-1}. \tag{25}$$

The predicted measurements will firstly pass to the modified state jumping detection part for innovation calculation, and then pass to the measurement update part for error covariance update.

3.3 Modified state jumping detection

The filter innovation $\boldsymbol{\varepsilon}_k$ can be used for state jumping detection, which is composed of the difference between the actual measurement and the predicted measurement:

$$\boldsymbol{\varepsilon}_k = \boldsymbol{y}_k - \hat{\boldsymbol{y}}_{k/k-1} \tag{26}$$

where $\boldsymbol{y}_k$ denotes the actual measurement. During the non-state-jumping period, the filter works in normal mode, and the value of the innovation is low. When a state jumping happens, the innovation will increase because of the mismatch between the nominal UKF dynamic model and the actual state jumping. Thus, a state jumping can be declared when innovation growth exceeds a predetermined level. Considering that orbit element errors vary in magnitude, a normalization of the innovation should be done for a concise state jumping detection. Thus, the dimensionless indicator γ_k is defined as

$$\gamma_k = \left(\boldsymbol{\varepsilon}_k^{\mathrm{T}}\boldsymbol{R}_k^{-1}\boldsymbol{\varepsilon}_k\right)^{1/2} \tag{27}$$

where $\boldsymbol{R}_k$ denotes the measurement noise covariance matrix. With $\boldsymbol{\varepsilon}_k \triangleq [\varepsilon_{k,1}, \varepsilon_{k,2}, \cdots, \varepsilon_{k,n_s}]$ and $\boldsymbol{R}_k \triangleq \mathrm{diag}\left(\left[R_{k,1}^2, R_{k,2}^2, \cdots, R_{k,n_s}^2\right]\right)$, (27) becomes

$$\gamma_k = \sqrt{\sum_{i_s=1}^{n_s} \frac{\varepsilon_{k,i_s}^2}{R_{k,i_s}^2}}. \tag{28}$$

When state jumping does not occur, according to the three-sigma rule, there is a 99.74% probability that $\varepsilon_{k,i_s} \leqslant 3R_{k,i_s}$. Thus, the threshold can be set as $\varGamma = 3\sqrt{n_s}$ to ensure the algorithm responds to various state jumping and possesses robustness against measurement noises. The setting of the threshold is independent of the measurement noise covariance matrix but relates to the dimension of measurements. Equation (10) indicates that the dimension of the measurements is six and we have $\Gamma = 3\sqrt{6}$.

When state jumping happens, the filter will diverge if the error covariance remains relatively constant. Therefore, when the indicator exceeds the threshold, the inflation of the covariance should be done to make the filter respond to the state jumping and re-converge to the new state. Considering that the magnitude of the covariance matrix is positively correlated with the convergence speed, set $\boldsymbol{S}_{k-1/k-1} = \boldsymbol{S}_{0/0}$ when state jumping happening is a viable option. This enables most state jumping to converge quickly, as demonstrated by the Monte Carlo simulations in Section 4. Since the data received by the receiver is discrete, and the time delay always exists for the state jumping detection, there usually exists a relatively large estimation error at the time instance when the state jumping is detected, especially for large state jumping. Thus, modification is made to reduce the estimation error at that time instance by re-conducting the previous procedures from (20) to (25) before proceeding to the measurement update.

3.4 Measurement update

Use the cross error covariance matrix $\boldsymbol{P}^{xy}_{k/k-1}$ and the predicted measurement error covariance square root $\boldsymbol{S}_{y,k/k-1}$ to generate the Kalman gain:

$$\boldsymbol{K}_k = (\boldsymbol{P}^{xy}_{k/k-1}/\boldsymbol{S}^{\mathrm{T}}_{k/k-1})/\boldsymbol{S}_{k/k-1} \tag{29}$$

where

$$\begin{cases} \boldsymbol{P}^{xy}_{k/k-1} = \displaystyle\sum_{i_s=0}^{n_s+1} w^c_{i_s}(\boldsymbol{\chi}_{i_s,k/k-1} - \hat{\boldsymbol{x}}_{k/k-1})(\boldsymbol{y}_{i_s,k/k-1} - \hat{\boldsymbol{y}}_{k/k-1})^{\mathrm{T}} \\ \boldsymbol{S}_{y,k/k-1} = \mathrm{qr}\left(\left[\sqrt{w^c_1}(\boldsymbol{y}_{1:n_s+1,k/k-1} - \hat{\boldsymbol{y}}_{k/k-1}),\ \sqrt{\boldsymbol{R}_k}\right]\right) \end{cases}. \tag{30}$$

Then, the updated covariance matrix square root and state vector can be computed by (31), which will be passed to the k time instant.

$$\begin{cases} \boldsymbol{S}_{k/k} = \mathrm{qr}\left[\left[\sqrt{w^c_{i_s}}(\boldsymbol{x}_{0:n_s+1,k/k-1} - \hat{\boldsymbol{x}}_{k/k-1}) - \right.\right. \\ \qquad \left.\left. \boldsymbol{K}_k\sqrt{w^c_{i_s}}(\boldsymbol{y}_{0:n_s+1,k/k-1} - \hat{\boldsymbol{y}}_{k/k-1}), \boldsymbol{K}_k\sqrt{\boldsymbol{R}_k}\right]\right] \\ \hat{\boldsymbol{x}}_{k/k} = \hat{\boldsymbol{x}}_{k/k-1} + \boldsymbol{K}_k(\boldsymbol{y}_k - \hat{\boldsymbol{y}}_{k/k-1}) \end{cases} \tag{31}$$

To summarize, this paper introduces the state jumping detection based on state augmentation, and the KF is modified with covariance matrix inflation and an additional one-step time update. Comparing with [22] and standard UKF, the distinguished contribution is labeled using the gold marker as shown in Fig. 1. Finally, with the utilization of MASUKF, the mean orbital elements are given as well as the unexpected state-jumping-thrust-acceleration, which is always assumed to be known in employing traditional UKF.

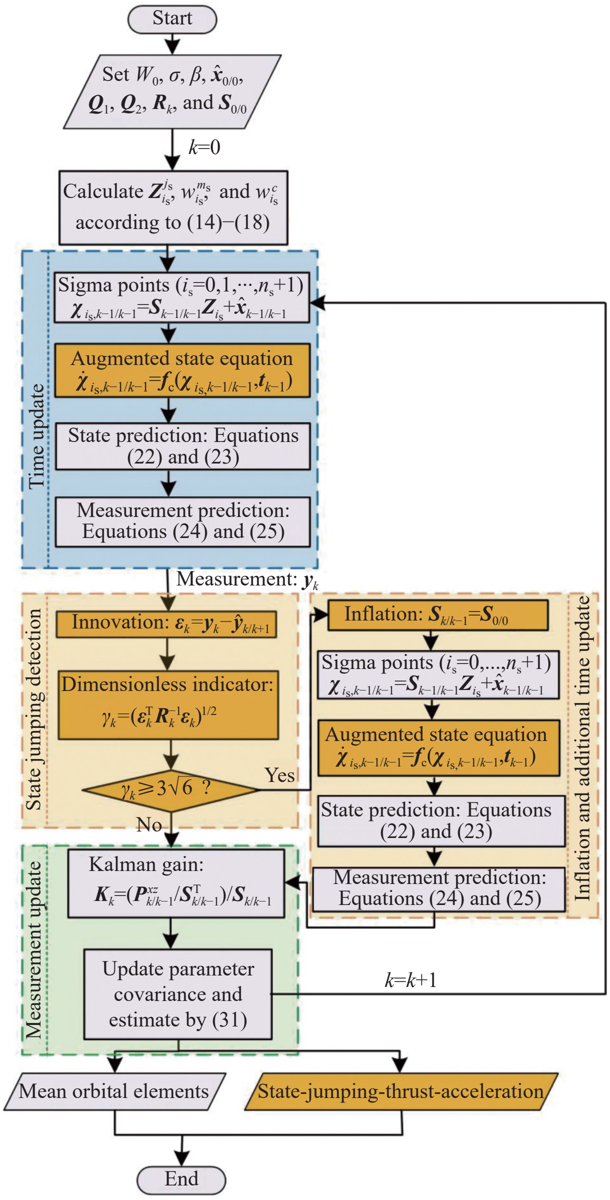

Fig. 1 Procedures of the MASUKF-based MOEs estimator

4. Simulations and results

The purpose of this section is to evaluate the performance of the MOEs estimator proposed in Section 3. Initially, a sample single run is done to intuitively show the estimate results and the variation of the state-jumping-detection-indicator. Then, comparisons among MASUKF, ASUKF, SRUKF, and DM method are conducted to demonstrate the advantage of the MASUKF-based MOEs estimator. Finally, Monte Carlo simulations are done for accuracy and state-jumping-detection-delay-time analysis.

4.1 Initial conditions and parameter values

The duration of the MOEs estimation task is assumed as one day, and the initial MOEs are given in Table 1. The NRLMSISE-00 model is then used to generate the initial atmospheric density ρ_0. With index $F_{10.7} = 150$ (the solar radio flux at 10.7 cm) and the geomagnetic coefficient $k_{\mathrm{P}} = 5$, it gives $\rho_0 = 2.72\times10^{-12}$ kg/m^3. The other parameters of the atmosphere drag model are $C_{\mathrm{D}} = 2.2$, and $H = 52.4$ km. The aerodynamic parameters are $m = 10$ kg and $S_1 = S_2 = 0.25$ m^2. The parameters of the MASUKF are $\sigma = 1$, $\beta = 2$, and $W_0 = 0.25$.

Table 1 Initial MOEs values

Parameter	Value
Semi-major axis/km	6 878.14
Eccentricity	0.02
Inclination/(°)	45
RAAN/(°)	20
Argument of the periapsis/(°)	20
Mean anomaly/(°)	20

Assume GNSS receiver is used to generate initial measurements, which can directly provide the instantaneous position, velocity and time information of the satellite, so it does not need to process the original pseudorange or carrier information. The one-sigma three-dimensional velocity and position errors are assumed as 2 cm/s and 5 m, respectively. The projection of the position and velocity measurement noise covariance onto OOEs space can be obtained utilizing the Monte Carlo analysis, yielding the results: $R_a^2 = 477.8$ m^2, $R_e^2 = 6.036\times10^{-12}$, $R_i^2 = 1.257\times10^{-12}$ rad^2, $R_\Omega^2 = 2.481\times10^{-12}$ rad^2, $R_\omega^2 = 1.496\times10^{-8}$ rad^2, $R_M^2 = 1.497\times10^{-8}$ rad^2. The discretized process noise are $Q_a^2 = 10^{-10}$ m^2, $Q_e^2 = 10^{-16}$, $Q_i^2 = 3\times10^{-20}$ rad^2, $Q_\Omega^2 = 3\times10^{-22}$ rad^2, $Q_\omega^2 = 3\times10^{-19}$ rad^2, $Q_M^2 = 3\times10^{-18}$ rad^2, $Q_{\mathrm{T}}^2 = Q_{\mathrm{N}}^2 = Q_{\mathrm{W}}^2 = 10^{-20}$ m/s^2. The covariance matrices $\boldsymbol{R}_k$ and $\boldsymbol{Q}_k$ are given by

$$\begin{cases} \boldsymbol{R}_k = \mathrm{diag}\left(R_a^2, R_e^2, R_i^2, R_\Omega^2, R_\omega^2, R_M^2\right) \\ \boldsymbol{Q}_k = \mathrm{diag}\left(Q_a^2, Q_e^2, Q_i^2, Q_\Omega^2, Q_\omega^2, Q_M^2, Q_{\mathrm{N}}^2, Q_{\mathrm{T}}^2, Q_{\mathrm{W}}^2\right) \end{cases}. \tag{32}$$

4.2 Estimation results of MOEs and state-jumping-acceleration

The numerical simulation starts by evaluating the MOEs-capture-ability of the estimator when state jumping happens. Assuming that the satellite cannot know the factors that cause state jumps, only the measured OOEs are given for MOEs estimation, which means autonomous detection of state jumping is required. Moderate and drastic regime jumps are analyzed. We utilize a low-thrust approach to simulate the moderate regime, applying a force of 0.004 N starting at 6 h into the simulation and lasting for a duration of 6 h. Conversely, the drastic regime is emulated using relatively high-thrust maneuvers, where a force of 0.5 N is exerted commencing at 18 h into the simulation and lasting for a duration of 1 min. The directions of the two thrusts are determined by the vectors $\left[\sqrt{3}/3,\ \sqrt{3}/3,\ \sqrt{3}/3\right]$ in the NTW coordinate system. The measured OOEs and the estimated MOEs (single run) are depicted in Fig. 2. It can be seen intuitively that the estimated MOEs can track the state jumping.

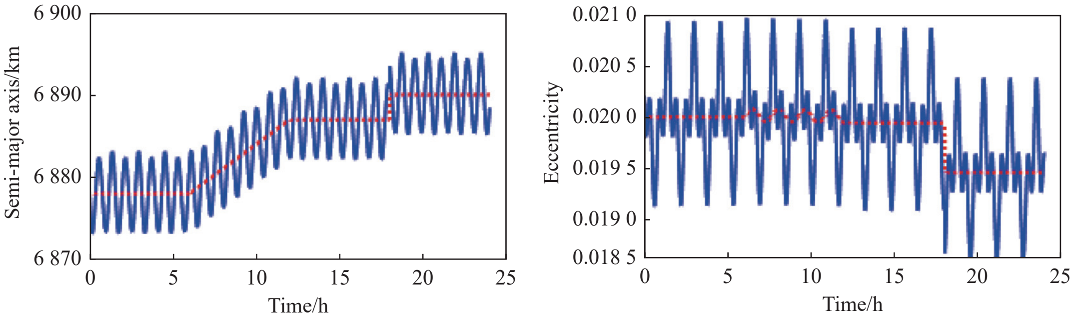

(a) Semi-major axis (b) Eccentricity

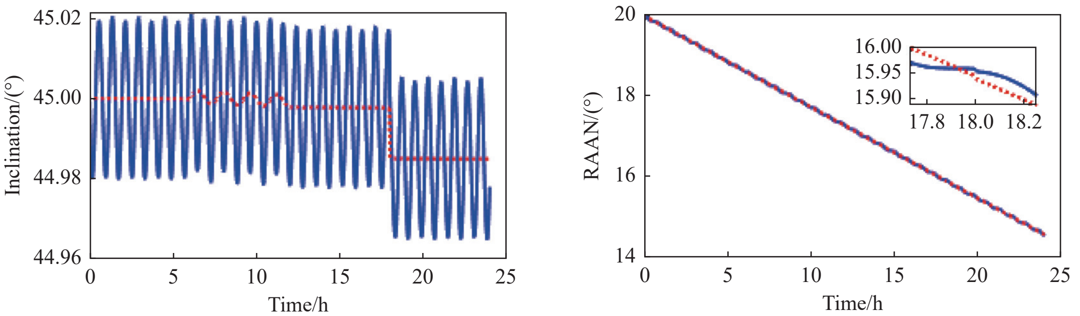

(c) Inclination (d) RAAN

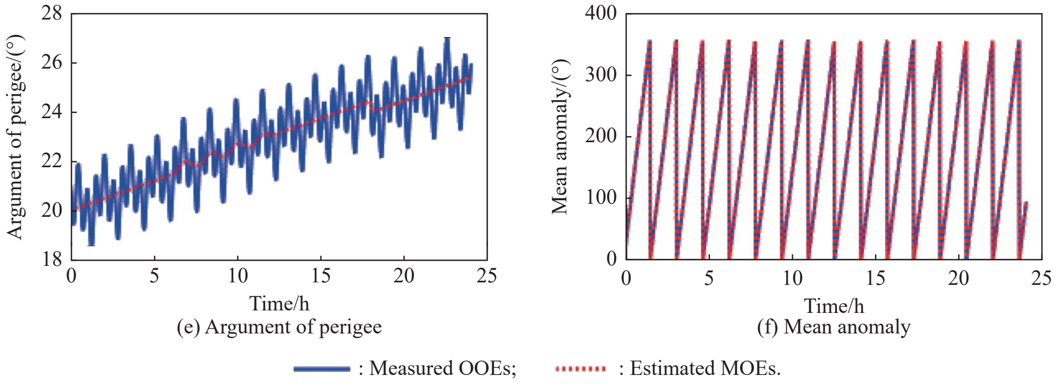

(e) Argument of perigee (f) Mean anomaly

Fig. 2 Sample single simulation comparing OOEs and estimated MOEs

The estimation error of the state-jumping-thrust-acceleration and the variation of the indicator are as shown in Fig. 3. The detected applied time of the low and high thrust is 6.05 h and 18.02 h, respectively. The detection of high-thrust is faster than low-thrust because the higher one will make the indicator hit the threshold faster. The detected end time is 12.05 h and 18.03 h for the low and high thrust, respectively.

The MASUKF estimator performance is compared to SRUKF, ASUKF and DM method. Fig. 4 shows the comparison between the mean-elements estimation errors obtained from SRUKF and MASUKF. Apparently, SRUKF diverges when a state jumping occurs and is hard to re-converge after the state jumping. Fig. 5 shows the comparison between the MOEs estimation errors gained from ASUKF and MASUKF. The main difference between ASUKF and MASUKF is that MASUKF inflates the covariance matrix when the indicator is greater than the threshold, and recalculates the predicted measurements before entering the measurement update step. However, ASUKF inflates the covariance matrix after detecting the state jumping and directly enters the next moment. Although the MASUKF is slightly more complicated than ASUKF when the indicator is greater than the threshold, Fig. 5 indicates that MASUKF estimates the MOEs for that period much better than ASUKF. The comparison between MASUKF and DM method is done using Mont Carlo simulation in Subsection 4.3.

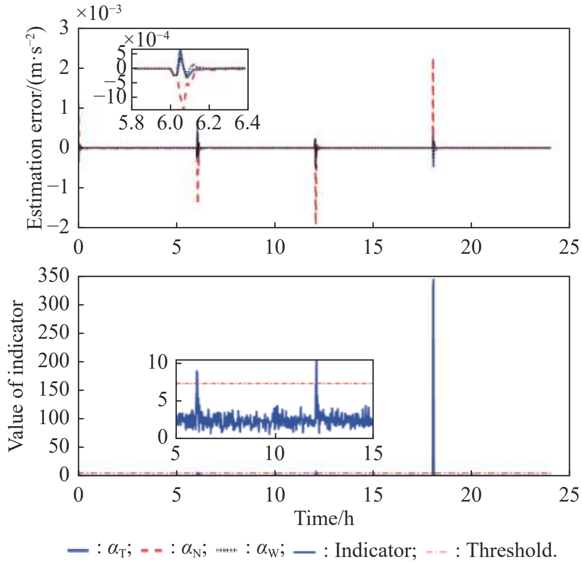

Fig. 3 Thrust acceleration estimation error and the variation of the indicator

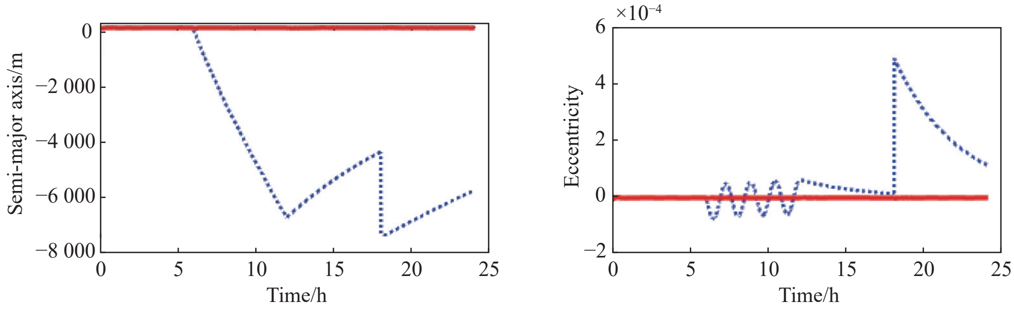

(a) Semi-major axis (b) Eccentricity

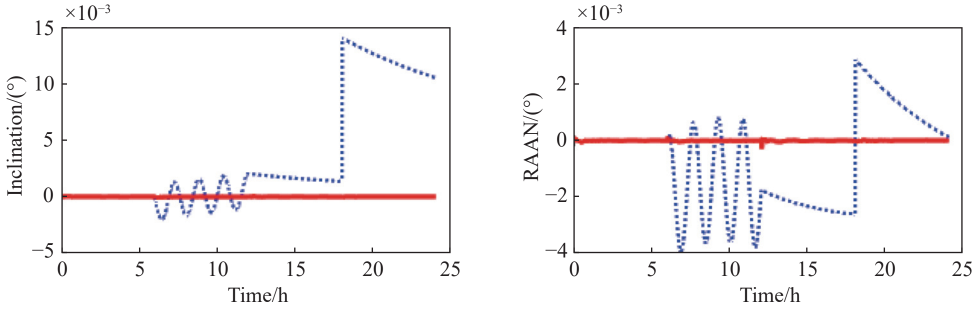

(c) Inclination (d) RAAN

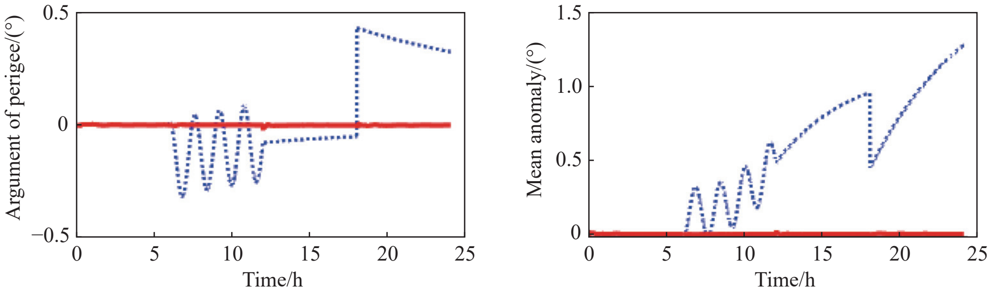

(e) Argument of perigee (f) Mean anomaly

······ : SRUKF; ▬ : MASUKF.

Fig. 4 Sample single simulation run comparing mean-elements estimation errors as obtained from SRUKF and MASUKF

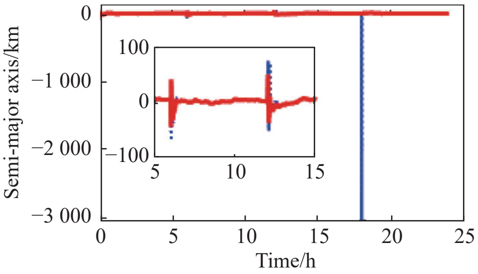

(a) Semi-major axis

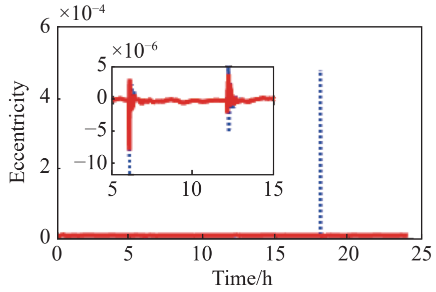

(b) Eccentricity

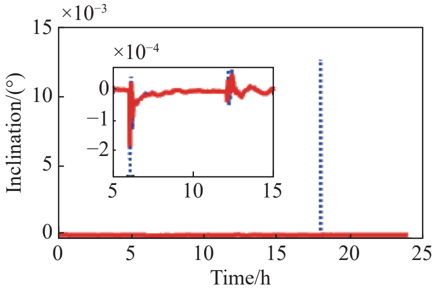

(c) Inclination

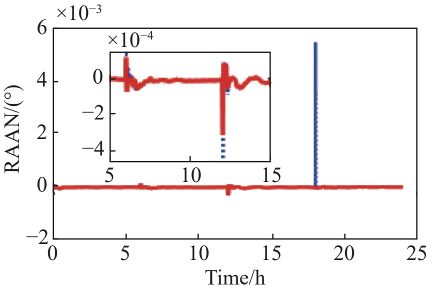

(d) RAAN

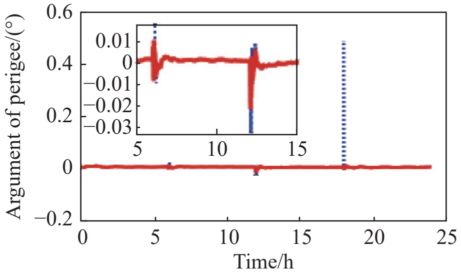

(e) Argument of perigee

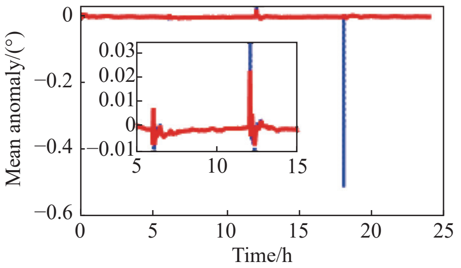

(f) Mean anomaly

······ : ASUKF; ▬ : MASUKF.

Fig. 5 Sample single simulation run comparing mean-elements estimation errors as obtained from ASUKF and MASUKF

4.3 Estimation accuracy and delay time analysis

Compared with the DM method, the accuracy of MASUKF is demonstrated. Root mean square error (RMSE) is obtained from 100 Monte Carlo simulations and used as a measure of estimator performance. The RMSE of each MOE at time t can be computed by

$$\boldsymbol{\varepsilon}_{\mathrm{r}}[j]=\sqrt{\frac{1}{100}\sum_{k=1}^{100}\left(\hat{\bar{\alpha}}[j]-\bar{\alpha}[j]\right)^2},\ j=1,2,\cdots,6 \quad (33)$$

where $\boldsymbol{\varepsilon}_{\mathrm{r}}=[\varepsilon_{\mathrm{r},a}(t),\varepsilon_{\mathrm{r},e}(t),\varepsilon_{\mathrm{r},i}(t),\varepsilon_{\mathrm{r},\Omega}(t),\varepsilon_{\mathrm{r},\omega}(t),\varepsilon_{\mathrm{r},M}(t)]^{\mathrm{T}}$, and k denotes the kth Mont Carlo simulation.

The estimated MOEs are $\hat{\bar{\boldsymbol{\alpha}}}=\left[\hat{\bar{a}},\hat{\bar{e}},\hat{\bar{i}},\hat{\bar{\Omega}},\hat{\bar{\omega}},\hat{\bar{M}}\right]^{\mathrm{T}}$. The true MOEs are $\bar{\boldsymbol{\alpha}}=\left[\bar{a},\bar{e},\bar{i},\bar{\Omega},\bar{\omega},\bar{M}\right]^{\mathrm{T}}$.

The RMSE of MASCKF and DM methods are shown in Fig. 6. The RMSE of the DM method is bigger than that of the MASCKF. Table 2 calculates and lists the average RMSE (ARMSE) in the time domain.

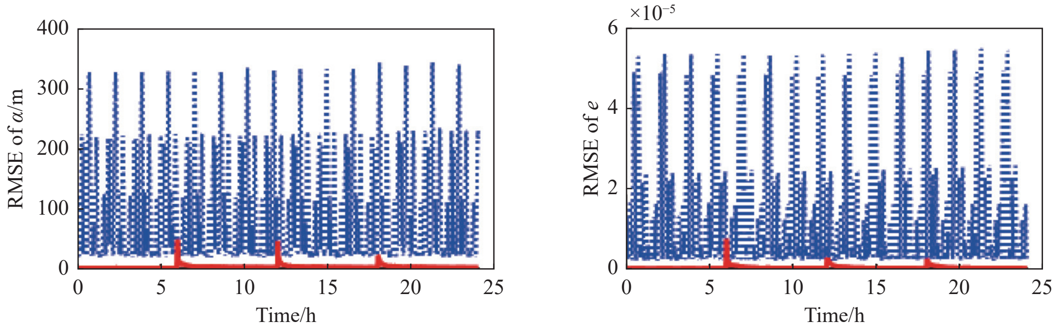

(a) Semi-major axis RMSE (b) Eccentricity RMSE

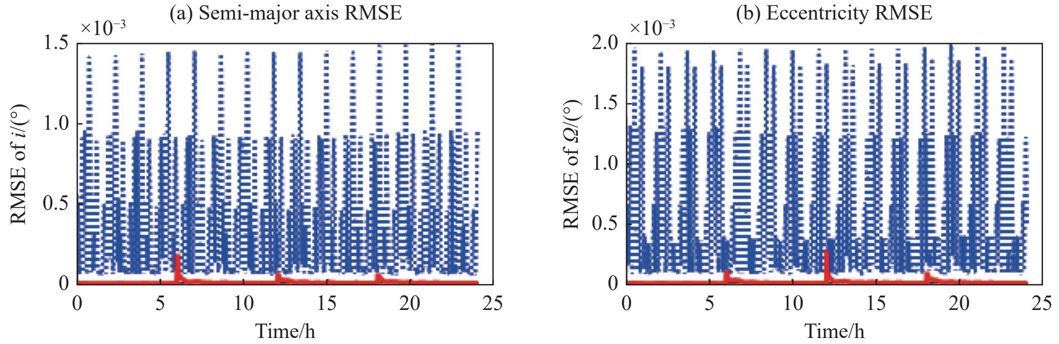

(c) Inclination RMSE (d) RAAN RMSE

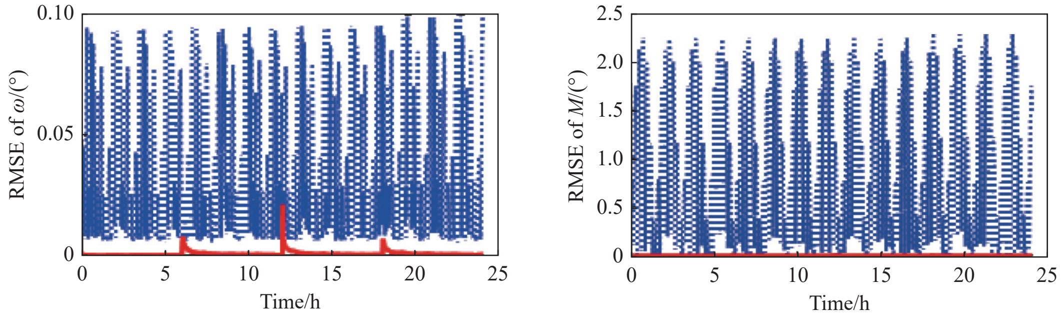

(e) Argument of periapsis RMSE (f) Mean anomaly RMSE

······· : DM; ▬ : MASUKF.

Fig. 6 Comparison between RMSE of estimated MOEs using MASUKF and DM method

Table 2 ARMSE of MASUKF and DM method

ARMSE parameter	Method	
	MASUKF	DM
Semi-major axis/m	2.855	104.1
Eccentricity	2.439×10^{-7}	1.421×10^{-5}
Inclination/(°)	6.110×10^{-6}	4.292×10^{-4}
RAAN/(°)	8.797×10^{-6}	6.311×10^{-4}
Argument of the periapsis/(°)	6.703×10^{-4}	3.677×10^{-2}
Mean anomaly/(°)	7.027×10^{-4}	0.955 1

The RMSE of the MASUKF and the DM method are computed for different thrust combinations. Select 100 combinations, the relative-long-duration-thrust within 0.01−0.5 N, and the approximate-impulse-thrust within 0.1−50 N. These thrusts are selected randomly and conform to uniform distribution within their corresponding intervals. The duration of the task is 12 h. Assume a sustained thrust of relatively long duration commencing at 3 h into the simulation and persisting for 3 h. Additionally, envision a brief burst of thrust with an approximate impulse applied at 9 h into the simulation, lasting for just 1 min. Other assumptions are unchanged. As shown in Fig. 7, MASUKF can deal with various situations, and usually gives better estimation results than the DM method. Fig. 7 also shows that the RMSE of the MASUKF result is large when the approximate-impulse-thrust is applied. This is due to that some approximate-impulse-thrust can make huge trajectory change within the time step (60 s), but the filter needs to converge gradually after the state jumping is detected. In practice, it is difficult to have such a large state jumping, and the MASUKF may usually perform better than the DM method at the start moment of the state-jumping. The ARMSE parameters in the time domain are calculated and listed in Table 3.

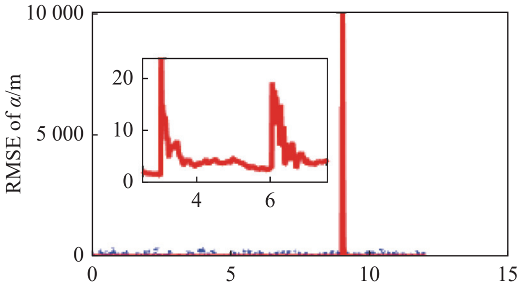

(a) Semi-major axis RMSE

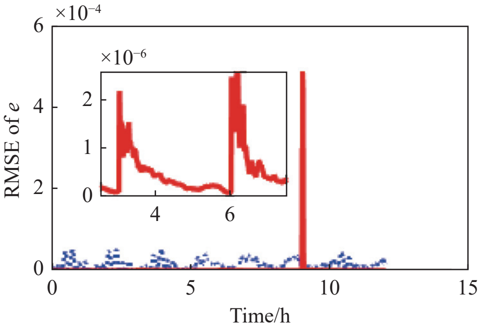

(b) Eccentricity RMSE

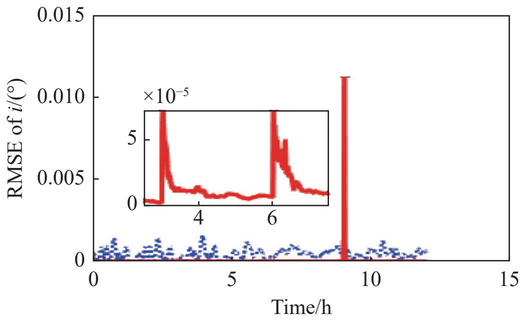

(c) Inclination RMSE

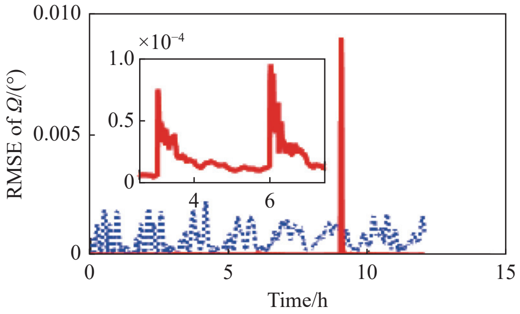

(d) RAAN RMSE

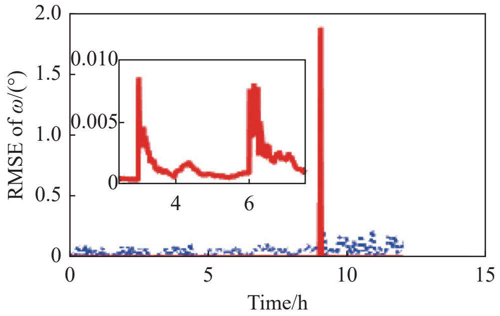

(e) Argument of periapsis RMSE

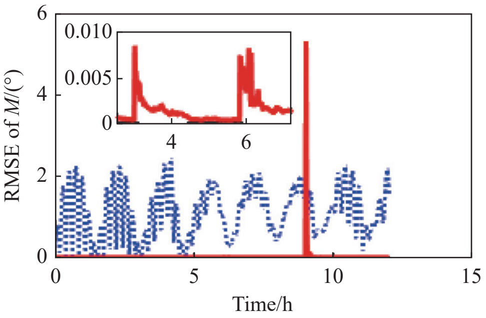

(f) Mean anomaly RMSE

┈┈ : DM; ━━ : MASUKF.

Fig. 7 RMSE comparison between DM method and MASUKF

Table 3 ARMSE of MASUKF and DM method in the time domain

ARMSE parameter	Method	
	MASUKF	DM
Semi-major axis/m	3.655	127.3
Eccentricity	3.529×10^{-7}	1.747×10^{-5}
Inclination/(°)	9.440×10^{-6}	5.167×10^{-4}
RAAN/(°)	1.415×10^{-5}	7.648×10^{-4}
Argument of periapsis/(°)	1.050×10^{-3}	6.480×10^{-2}
Mean anomaly/(°)	1.105×10^{-4}	1.210

The MASUKF will process several steps to converge to the new orbit as soon as detecting the state jumping, which means the detection part of the MASUKF is essential. Thus, the delay time of the detection is analyzed. There are mainly four parameters to be considered in the delay time analysis: the direction of the state-jumping-thrust-acceleration, the magnitude of the state-jumping-thrust-acceleration (a_{sj}), the start time of the state jumping, and the time step of the estimator. To present the data in a concise manner, the direction of the state-jumping-thrust-acceleration and the start time of the state jumping are assumed fixed. Fig. 8 depicts the variation of the delay time with the time step and the magnitude of the state-jumping-thrust-acceleration. The projection on the *XZ*, *YZ* plane and the contour lines on the *XY* plane are also depicted in Fig. 8. As the acceleration-magnitude increases, the delay time decreases. When the delay time is bigger than the time step, the delay time is not obviously influenced by the time step. Otherwise, the delay time is equal to the time step. However, if we use the number of the time steps contained in the delay time to reflect the delay characteristic of the detection, we can make a conclusion that the delay of the detection is negatively related with both the acceleration-magnitude and the time step as shown in Fig. 9.

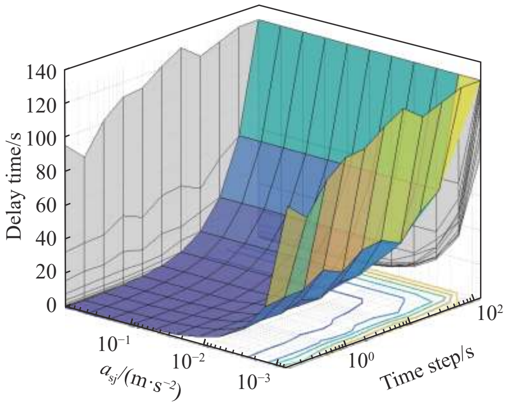

Fig. 8 Variation of delay time with time step and magnitude of state-jumping-thrust-acceleration

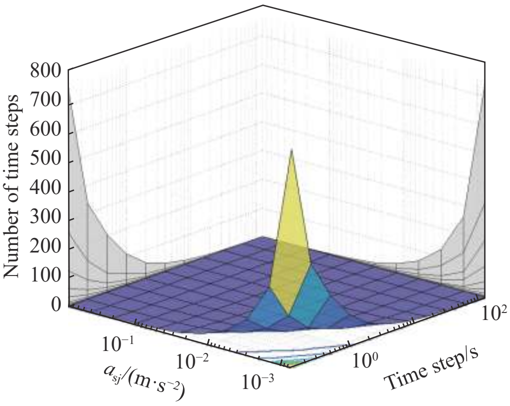

Fig. 9 Variation of the number of time steps contained in delay time with time step and magnitude of state-jumping-thrust-acceleration

5. Conclusions

In this paper, the issue of MOEs estimation under state jumping condition is discussed. A novel MASUKF is proposed to deal with this issue. It can detect state jumping, obtain real-time MOEs, estimate state-jumping-thrust-acceleration, and significantly decrease the estimation error at the detection moment. The numerical simulation shows that the filter can provide better estimated MOEs than the SRUKF, the ASUKF, and the DM method. Additionally, when various state jumping happens, the MASUKF can usually detect them with low latency, and track them. Consequently, the accurate and efficient MASUKF estimator proposed in this paper is suitable for onboard MOEs estimation with state jumping.

References

[1] CAO X, LI N, QIU S, et al. Research on the method of searching and tracking of the time-sensitive target through the mega-constellation. Aerospace Science and Technology, 2023, 137: 108299.

[2] INIGO D P, BRUCE G C, EDWARD F C. A technical comparison of three low earth orbit satellite constellation systems to provide global broadband. Acta Astronautica, 2019, 159(6): 123–135.

[3] TAO X F, LI Z, XU C, et al. Track-to-object association algorithm based on TLE filtering. Advances in Space Research, 2021, 67(8): 2304–2318.

[4] KUAI Z Z, CAO X L, SHEN H X, et al. Maneuver planning of geostationary satellites using mean orbital elements. Proc. of the Chinese Automation Congress, 2020: 6596−6600. (in Chinese)

[5] PAN X, XU M, DONG Y F. Low-thrust displaced orbits by weak Hamiltonian-structure-preserving control. Communications in Nonlinear Science and Numerical Simulation, 2018, 62(9): 282–306.

[6] ASRAF A, SURAYUDA R H, RIBAH A Z, et al. Determination of mean orbital elements using GPS data for LAPAN satellite daily operation. Proc. of the IEEE International Conference on Aerospace Electronics and Remote Sensing Technology, 2021. DOI: 10.1109/ICARES53960.2021.9665177.

[7] KOZAI Y. The motion of a close Earth satellite. Astronomical Journal, 1959, 64(11): 367–377.

[8] KOZAI Y. Effect of precession and nutation on the orbital elements of a close earth satellite. Astronomical Journal, 1960, 65(10): 621–623.

[9] BROUWER D. Solution of the problem of artificial satellite theory without drag. Astronomical Journal, 1959, 64(11): 378–396.

[10] CHEN H Y, WU H Y, ZHOU M J, et al. Orbit engineering application and STK simulation for micro-satellite. Beijing: China Science Publishing & Media Ltd., 2016. (in Chinese)

[11] SETTY S, CEFOLA P, MONTENBRUCK O, et al. Application of semi-analytical satellite theory orbit propagator to orbit determination for space object catalog maintenance. Advances in Space Research, 2016, 57(10): 2218–2233.

[12] DUTT P, ANILKUMAR A K. Orbit propagation using semi-analytical theory and its applications in space debris field. Astrophysics and Space Science, 2017, 362: 35.

[13] LARA M, SAN J F, HAUTESSERRES D, et al. A mean elements orbit propagator program for highly elliptical orbits. CEAS Space Journal, 2018, 10(5): 3−23.

[14] NIE T, GURFIL P. Reducing inter-satellite drift of low Earth

orbit constellations using short-periodic corrections. Celestial Mechanics and Dynamical Astronomy, 2021, 133: 19.

[15] VNIE T, GURFIL P. Long-term evolution of orbital inclination due to third-body inclination. Celestial Mechanics and Dynamical Astronomy, 2021, 133: 1.

[16] JULIER S, UHLMANN J K, DURRANT-WHYTE H. A new approach for filtering nonlinear systems. Proc. of the American Control Conference, 1995: 1628−1632.

[17] MERWE R, WAN E. The square-root unscented Kalman filter for state and parameter-estimation. Proc. of the IEEE International Conference on Acoustics, 2001: 3461−3464.

[18] LI K Y, GUO Z K, ZHOU G J. State estimation in range coordinate using range-only measurements. Journal of Systems Engineering and Electronics, 2022, 33(3): 497–510.

[19] GONG B C, WANG S, HAO M R, et al. Range-based collaborative relative navigation for multiple unmanned aerial vehicles using consensus extended Kalman filter. Aerospace Science and Technology, 2021, 112: 106647.

[20] WANG K, CHEN T, XU S J. Determination and estimation of differential mean orbital elements for formation-flying missions. Journal of Guidance, Control, and Dynamics, 2014, 37(1): 86–97.

[21] WANG K, CHEN T, XU S J. A comparison of algorithms for computing differential mean orbital elements in formation flying missions. Proc. of the AIAA Guidance, Navigation, and Control Conference, 2013. DOI: 10.2514/6.2013-4542.

[22] ZHONG W C, GURFIL P. Mean orbital elements estimation for autonomous satellite guidance and orbit control. Journal of Guidance, Control, and Dynamics, 2013, 36(6): 1624–1641.

[23] LI L C, ZHANG J R, ZHAO S G, et al. Autonomous onboard estimation of mean orbital elements for geostationary electric-propulsion satellites. Aerospace Science and Technology, 2019, 94: 105369.

[24] ZHAI G, ZHAO H Y, WEN Q Q, et al. Relative motion and thrust estimation of a non-cooperative maneuvering target with adaptive filter. Acta Astronautica, 2019, 162(9): 98–108.

[25] WANG Y D, SUN S M, LI L. Adaptively robust unscented Kalman filter for tracking a maneuvering vehicle. Journal of Guidance, Control, and Dynamics, 2014, 37(5): 1696–1701.

[26] JIANG Y Z, BAOYIN H X, MA P B. Augmented unbiased minimum-variance input and state estimation for tracking a maneuvering satellite. Acta Astronautica, 2019, 163: 96–107.

[27] KO H C, SCHEERES D J. Orbit determination across unknown maneuvers using the essential thrust-Fourier-coefficients. Acta Astronautica, 2016, 118(1/2): 90–95.

[28] ZHAI G, BI X Z, ZHAO H Y, et al. Non-cooperative maneuvering spacecraft tracking via a variable structure estimator. Aerospace Science and Technology, 2018, 79(8): 352–363.

[29] NASTASI K M, BLACK J T. Adaptively tracking maneuvering spacecraft with a globally distributed, diversely populated surveillance network. Journal of Guidance, Control, and Dynamics, 2019, 42(5): 1033–1048.

[30] YU Y J, YUE C F, LI N, et al. Onboard estimation of mean orbital elements extended to state jumping case. Journal of Guidance, Control, and Dynamics, 2022, 45(11): 1996–2012.

[31] LIU L, TANG J S. Satellite orbit theory and application. Beijing: Publishing House of Electronics Industry, 2015. (in Chinese)

[32] SCHAUB H, ALFRIEND K. Impulsive feedback control to establish specific mean orbit elements of spacecraft formations. Journal of Guidance, Control, and Dynamics, 2001, 24(4): 739–745.

[33] BATTIN R. An introduction to the mathematics and methods of astrodynamics. Reston: AIAA Education Series, 1999.

[34] JULIER S. The spherical simplex unscented transformation. Proc. of the American Control Conference, 2003: 2430−2434.

Biographies

YU Yanjun was born in 1995. She received her B.S. and M.S. degrees from Harbin Institute of Technology, China, in 2018 and 2020, respectively. She is currently pursuing her Ph.D. degree with the School of Astronautics, Harbin Institute of Technology, China. She is also a visiting Ph.D. student in the Department of Aerospace Science and Technology of Politecnico di Milano. Her main research interests include orbital dynamics, navigation, constellation design, and constellation control.

E-mail: yuyanjun9511@163.com

YUE Chengfei was born in 1989. He received his B.E. degree in spacecraft design and engineering from Harbin Institute of Technology, Harbin, China, in 2013, and Ph.D. degree in electrical and computer engineering from the National University of Singapore, Singapore, in 2019. He is currently a professor with Harbin Institute of Technology (Shenzhen) (HITSZ), Shenzhen, China, where he is also the director of the Advanced Space Application and Intelligent Control Lab. His main research interests include high-performance control and on-orbit service.

E-mail: yuechengfei@hit.edu.cn

LI Huayi was born in 1978. He received his M.S. and Ph.D. degrees in control science and engineering from Harbin Institute of Technology, China, in 2004 and 2008, respectively. Currently, he is a full professor in spacecraft design with Harbin Institute of Technology, Harbin, China, and the director in Research Center of Satellite Technology with Harbin Institute of Technology, Harbin, China. His main research interests include autonomous distributed space systems, space remote sensing and satellite electronic testing.

E-mail: lihuayi@hit.edu.cn

WU Yunhua was born in 1981. He received his B.S., M.S., and Ph.D. degrees in aerospace engineering from Harbin Institute of Technology, in 2004, 2006, and 2009, respectively. Since 2013, he has been a professor with the School of Astronautics, Nanjing University of Aeronautics and Astronautics. His main research interests include space vehicle design, mission analysis, space vehicle dynamics and control, and hardware-in-the-loop simulation.

E-mail: yunhuawu@nuaa.edu.cn

CHEN Xueqin was born in 1982. She received her Ph.D. degree in control science and engineering from Harbin Institute of Technology, China, in 2008. She is currently a professor in aircraft design and engineering with Harbin Institute of Technology, Harbin, China. Her main research interests are fault diagnosis and fault-tolerant control.

E-mail: cxqhit@163.com